Applied Surface Science 573 (2022) 151612

Contents lists available at ScienceDirect

Applied Surface Science

journal homepage: www.elsevier.com/locate/apsusc

Full Length Article

Long-term seawater anti-corrosion properties of Al alloy triggered by femtosecond laser structuring with phase change

Rahul A. Rajan [a,b], Srinivasa Rao Konda [a], Chaudry Sajed Saraj [a,b], Yu Hang Lai [a], Gopal Verma [a], Zhi Yu [a,*], Weili Yu [a], Dandan Yan [a,b], Jianjun Yang [a,*]

[a] GPL, Changchun Institute of Optics, Fine Mechanics and Physics, Chinese Academy of Sciences, Changchun 130033, China
[b] University of Chinese Academy of Science, Beijing 100039, China

ARTICLE INFO

Keywords:
Femtosecond laser processing
Superhydrophobic surface
Stable oxide layers
Laser-induced phase change
Long-term corrosion resistance in seawater

ABSTRACT

Through adopting a technique of femtosecond laser micro/nano-structuring, we successfully modify the surface of aluminium alloy material into the long-term stable anti-corrosive properties, exhibiting the measured corrosion rate two orders of magnitude smaller than that of the bare sample. The underlying mechanisms are attributed to both the surface micro/nano-structure formation with the thick stable oxide layers and the significant phase change from crystalline to amorphous by the laser-induced stress and compressive strain, which consequently reduce the free energy and chemical activity of the structured surface. Such investigations may open a new eco-friendly way to produce anti-corrosive metal surfaces for deep seawater applications.

1. Introduction

Aluminium alloys are widely used metals in engineering fields due to their superior mechanical, chemical and physical properties [1,2]. Their lightweight nature, low density (only 2.7 g/cm^3) and intrinsic corrosion resistance offer an unique importance in various deep seawater applications such as naval architectures and ocean equipment manufacturing [3]. However, the abundant highly corrosive chloride and potassium ions in seawater can still corrode the inherent oxide layers on metal surfaces. It leads to penetrating failures, thereby limiting Al alloy's usage in marine applications [4]. As a result, the anti-corrosion research on Al alloy surfaces to avoid corrosive ions interaction is both life-saving and cost-effective [5,6]. Currently, the most often used surface engineering techniques include electroplating [7], galvanizing [8], anodizing [9], chemical deposition [10], carburizing [11], and thermal spraying [12]. However, all of them have several drawbacks, such as inefficient use of material, time, and energy, lack of precision and flexibility, and most critically, are ecologically unfriendly. Recently, laser processing techniques have been getting wide acceptance to improve the anticorrosion properties of metal surfaces from various corrosive environments [7–9]. In general, the previous studies tried to repel water and aggressive corrosive ions by making use of surface superhydrophobic (SHP) properties of micro/nano- structures with a combination of the chemical layer deposition [10–14]. However, the corrosion attack for the long-term immersing inside the corrosive medium like the seawater cannot be efficiently prevented, especially when the superhydrophobic properties began to disappear partially or completely with the lapse of time [8,15]. Therefore, how to achieve sustainable corrosion protection for the laser fabricated surface without any additional chemical layer treatments still remains a big challenge.

To the best of our knowledge, it is here for the first time to demonstrate the long-term seawater anti-corrosion behaviors for Al alloys through the crystalline-amorphous phase change induced by the femtosecond laser pulses. More interestingly, this result can help to overcome the anticorrosion instability issues when the surface superhydrophobicity disappears. The importance of the laser-induced highly stable oxide barrier layers was also investigated for protecting the substrate from corrosion attack. A comparison of our work with some recent reports based on the laser-induced corrosion protection is shown in Table S1. During our experiments, a sample of Al alloys (#6061) was firstly microstructured by femtosecond laser pulses with various scanning speeds. Subsequently, both the electrochemical impedance spectroscopy and potentiodynamic polarization measurements were carried out to explore the corrosion protection properties of the samples in the seawater. The obtained corrosion resistance is significantly increased to the order of MΩ and the corrosion current is dramatically decreased to as small as 3.0 nA cm^{-2}. Even after two months of continuous immersion in the seawater, the laser fabricated surfaces exhibited an excellent

* Corresponding authors.
E-mail addresses: zhiyu@ciomp.ac.cn (Z. Yu), jjyang@ciomp.ac.cn (J. Yang).

https://doi.org/10.1016/j.apsusc.2021.151612
Received 8 July 2021; Received in revised form 5 October 2021; Accepted 11 October 2021
Available online 16 October 2021

corrosion resistance with less corrosion current of 10.0 nA cm^{-2}. For the purpose of investigating anti-corrosion mechanisms, we performed X-ray diffraction (XRD) and transmission electron microscopy (TEM) analyses of the samples, which reveals the significant material phase change from the crystalline to partial amorphous with the thick stable oxide layer formation. Therefore, the femtosecond laser-induced robust corrosion protective surfaces can be allowed for deep-sea applications.

2. Experimental section

2.1. Fabrication of anti-corrosive micro/nano-structures by femtosecond laser pulses

In this study, we employed a Ti:Sapphire laser amplifier system (Spitfire Ace, Spectra-Physics) as a light source, which delivers femtosecond laser pulses at the repetition rate of 1 kHz, with the central wavelength of 800 nm and the pulse duration of 40 fs. The hierarchical micro/nano-structures were fabricated on the sample material containing the following chemical compositions (in weight %): Al- 79.87%, C- 7.55%, O- 4.98%, N- 3.35%, Se- 1.37%, F- 1.02%, Mg- 0.64%, Fe- 0.33%, Si- 0.22% and Na- 0.67%. The maximum pulse energy from the laser system can reach 6 mJ, and it was attenuated using the combination of a half-wave plate and a polarizer. The appropriate laser energy was then focused on the sample surface with a spherical lens (focal distance f = 200 mm) at normal incidence. The grid scanning of the samples was carried out via a computer-controlled 3D translational stage to generate the structures within an area of 13 mm × 13 mm. The focal laser beam spot on the sample surface was calculated around 50 μm in diameter. To get a stand-alone effect of the laser scanning speed, the whole study was carried out with a constant laser energy fluence of F = 15.3 J/ cm^2 and the spacing of 100 μm between two adjacent micro-grooves (step size).The laser scanning speed was varied as V = 0.4 mm/s, 0.6 mm/s, 0.8 mm/s and 1.0 mm/s. A schematic of femtosecond laser fabrication is shown in Fig. 1(a). After the laser processing, the fabricated samples were ultrasonicated for 1 hr with the deionized water and dried with the compressed air. These samples were superhydrophilic in nature, the transformation of their surface into the superhydrophobic was carried out by a simple annealing process at 200 °C for 2 hr in an air environment [16]. In all the experiments, both the surface characterizations and electrochemical measurements were performed on such post-processed samples.

2.2. Surface characterization and electrochemical measurements

Surface morphologies of the prepared samples were observed with a scanning electron microscope (SEM) (ProX-5, Phenom, Netherlands),

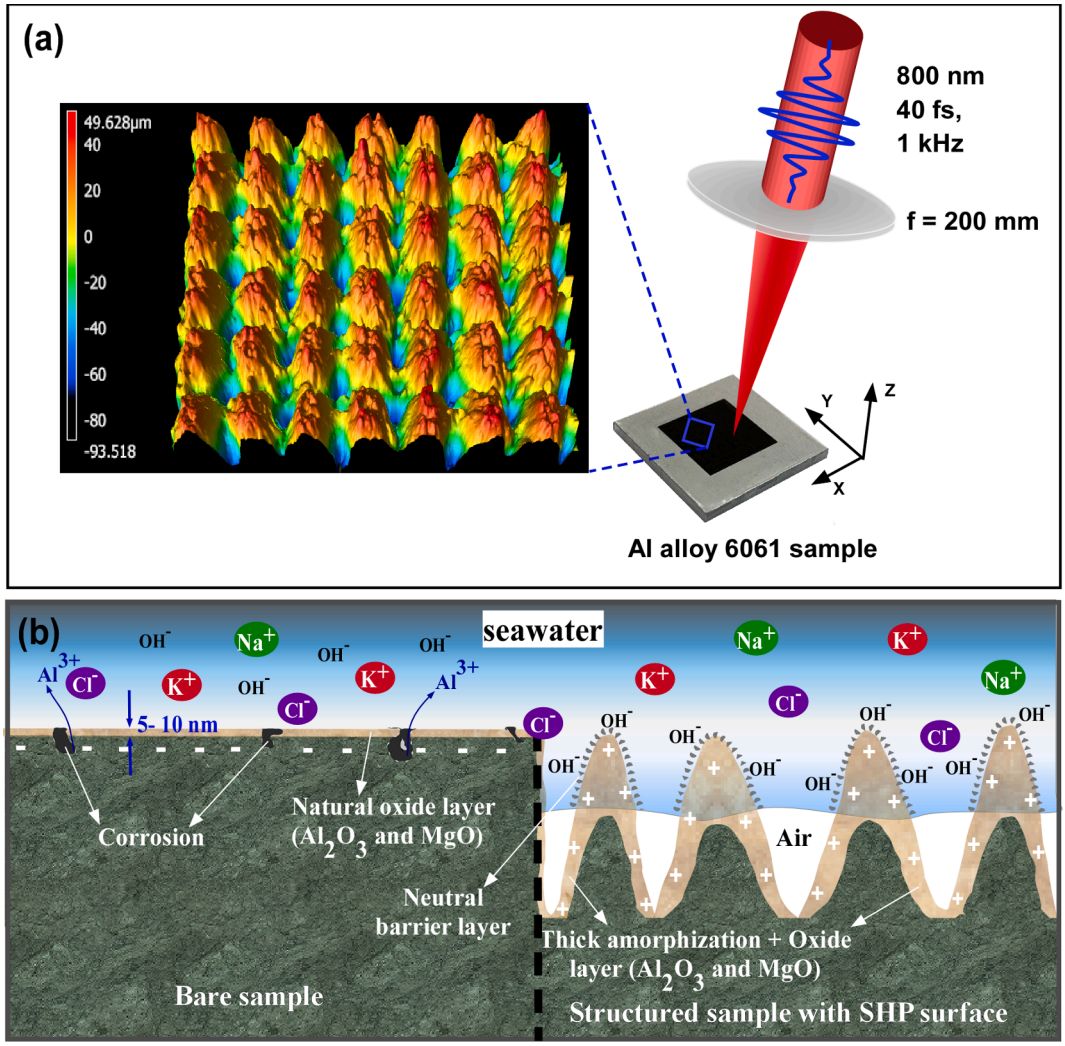

Fig. 1. (a) Schematic of the direct femtosecond laser fabrication and structured surface morphology ; (b)Illustrated corrosion of the bare sample surface and the anti-corrosion of the laser structured sample, because the latter case having a combined effect of the superhydrophobic, material amorphization and charge layer distribution at the metal oxide- electrolyte interface.

and the high-resolution SEM pictures were obtained under the acceleration voltage of 15 kV. All the energy-dispersive X-ray spectroscopy (EDS) spectra were also collected by mapping the electron beam at the same acceleration voltage. The characterization of surface wettability for the fabricated surfaces was performed by a contact angle measurement instrument (JC2000D3, POWEREACH, China) with a 5 μl seawater droplet. The droplets were dispensed at five different positions on the sample to get the average contact angle (CA) and sliding angle (SA) values.

The electrochemical measurements were performed using a Biologic VMP-3 workstation (VMP-3, BioLogic, France) to study the anti-corrosion properties of as-prepared samples. To make our corrosion experiments similar to the practical environment, we adopted the real seawater from the Dalian coast of the Yellow Sea, China for the electrolyte. The seawater is collected from a depth of no more than 5.0 m, whose chemical contents can be seen from the global analysis forecast BIO 001 028, Copernicus database (given in Table S2) [17]. All the measurements were carried out at room temperature with a three-electrode setup, and the as-prepared samples (having a laser-processed portion of 1.69 cm^2) are used as a working electrode for an exposed area of only 0.78 cm^2. We employed the Pt mesh as a counter electrode and silver/silver chloride (Ag/AgCl) as a reference electrode (within a fitted compartment surrounded by the saturated KCl solution with a potential of 0.197 V with respect to the standard hydrogen electrode (SHE) at 24 ± 1 °C). After 3 h of open circuit potential (OCP) test, the electrochemical impedance spectroscopy measurements were performed to compare the impedance behavior of the samples from an initial frequency of 200 kHz to a final frequency of 100 MHz, through an alternating current sine wave with the amplitude of 10 mV. The polarization curves were obtained with a potential range of −100 mV to +600 mV *vs.* OCP by using a scan rate of 10 mV.min^{-1}. The corrosion current density (I_{corr}) for all the studied samples was obtained by extrapolating the anodic and cathodic Tafel slopes. The experiments were repeated at least three times to confirm the reproducibility of all the electrochemical measurement results.

3. Results and discussion

3.1. Morphological characterization of femtosecond laser structured surfaces

The surface morphology of the laser fabricated structures on the Al alloy sample was studied in detail. Here we only took the results from the laser scanning speed of V = 0.4 mm/s as an example (the observations for other scanning speeds such as V = 0.6 mm/s, 0.8 mm/s, and 1.0 mm/s are shown in Fig. S1), as shown in Fig. 2(a)–(c). The periodic microgroove covered with the recast layer of the ablation materials appears to build the complex hierarchical structures and act as the efficient air pockets. The microhardness measurement revealed that the surface layer of the laser fabricated sample has a value of 45.9 HV, which is hardened by around 1.8 times relative to the bare sample. Moreover, the presence of nanoscale fringes and particles shown in Fig. 2(c) can help to reduce the possible solid–liquid interaction area by trapping atmospheric air inside. Its role in preventing the surface underneath from the further corrosion is discussed later.

In spite of fixing the beam spot size during the laser irradiation, the significant variations in both width and height of the microgrooves can take place with different scanning speeds, as shown in Fig. 2(e). While

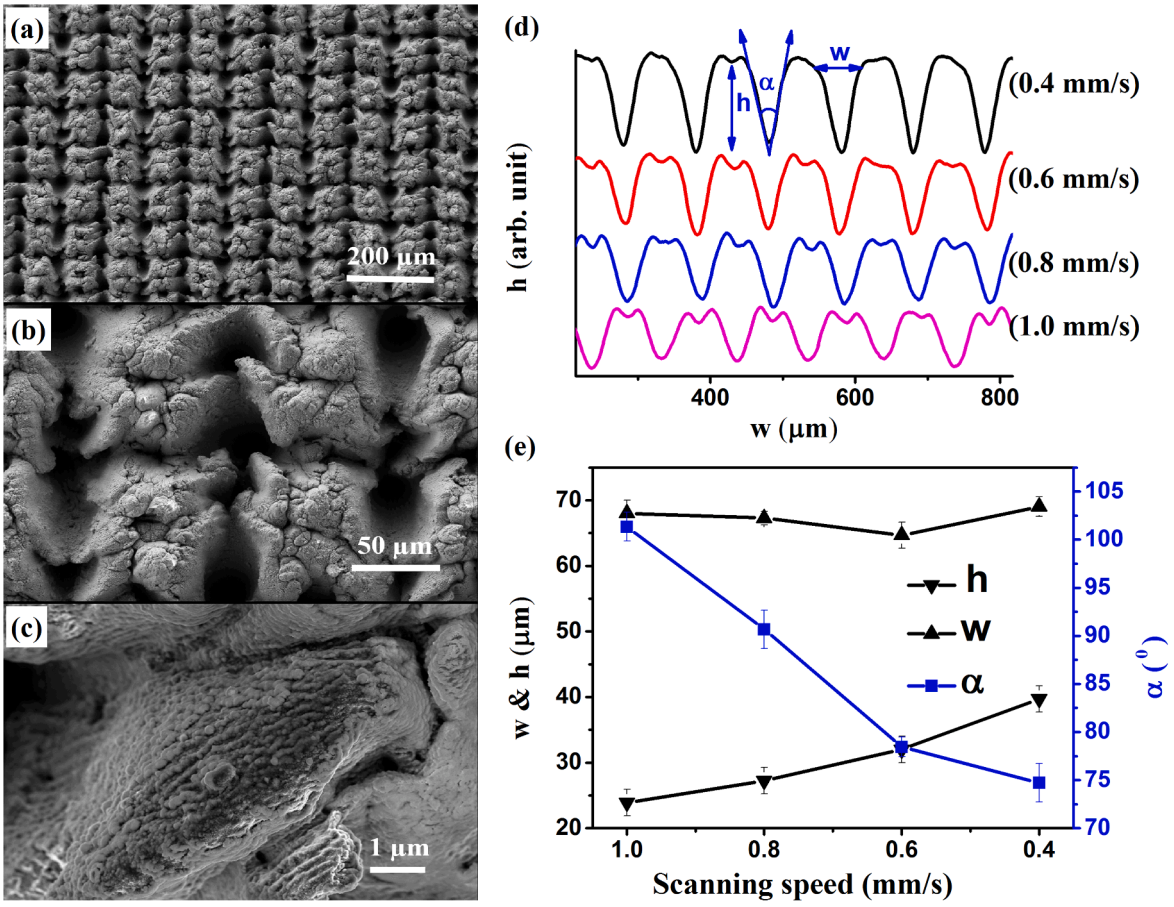

Fig. 2. (a) SEM images of the fabricated surface at the laser scanning speed of V = 0.4 mm/s; (b) Formation of air pockets in the micro-grooves; (c) Thick laser ablated recast material with complex micro/nano-structures; (d) Measured geometrical profiles the micro-groove lines; (e) Measured relationships between the width (w), height (h) and opening angle (α) of the grooves for the situations of different laser scanning speeds.

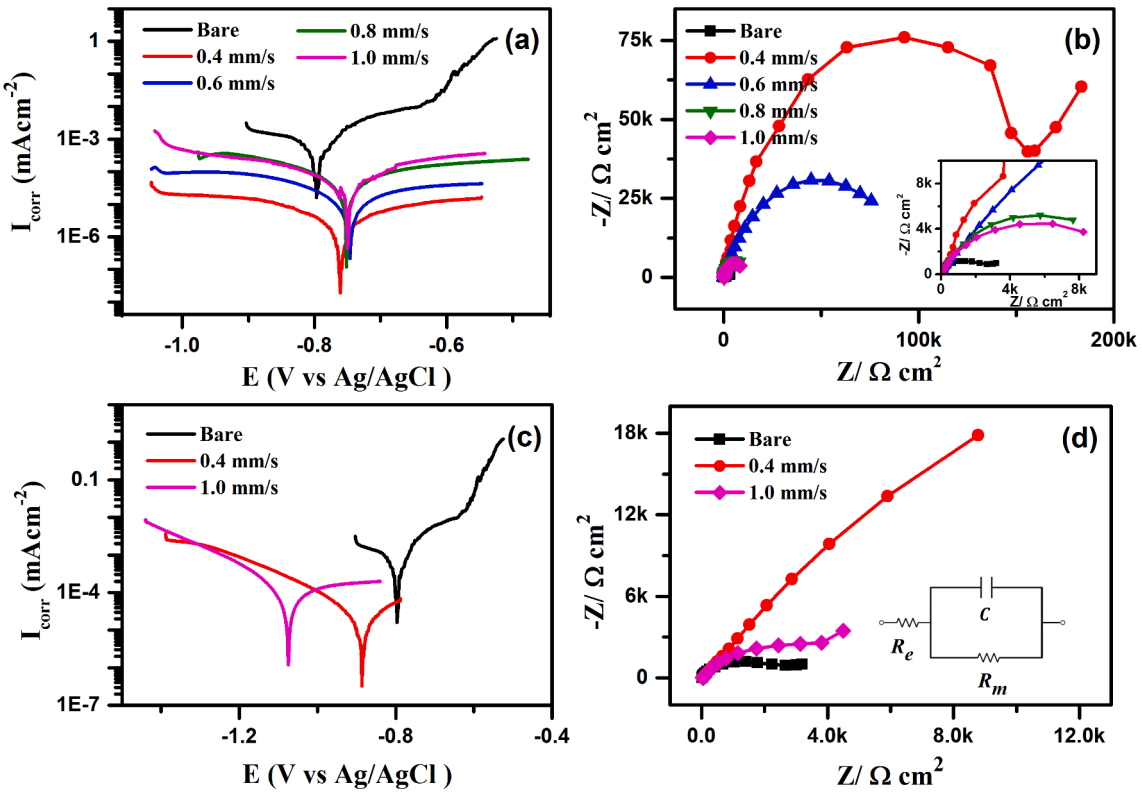

Fig. 3. Examined anticorrosive nature of the bare and fabricated sample surfaces with different laser scanning speeds: (a) Cyclic polarization curves and (b) Nyquist plots immediately after the laser fabrication. (c) and (d) for the measurements after the seawater immersion for two months.

changing the laser scanning speed from V = 1.0 mm/s to 0.4 mm/s, the microgroove height gradually increases because of the high ablation rate (being quantified as a ratio of the ablated microgroove depth to its width), whereas the groove width is kept almost constant. In general, the opening angle (α) of the fabricated grooves is reduced to result in a high aspect ratio, preventing the liquid penetration to the deeper grooves [18,19].

It was found that an increment in surface roughness can improve the superhydrophobic property of the laser fabricated surfaces at different scanning speeds, in which other experimental parameters were well maintained. The percentage of pulse overlapping (or the number of pulse accumulation) on the sample surface is determined by the laser scanning speed, which has the values of 99.2%, 98.8%, 98.4%, and 98.0% for V = 0.4 mm/s, 0.6 mm/s, 0.8 mm/s, and 1.0 mm/s, respectively. It was improved that the ablation rate increases with lower laser scanning speeds or higher overlapping factors, leading to the deeper microgrooves and the larger surface roughness (shown in Fig. S2(a)).

The superhydrophobic property of the laser fabricated sample was eventually achieved by lowering the surface energy through annealing process at 200 °C in air environment, because the micro or nano burrs of the structured surfaces can efficiently adsorb the airborne hydrocarbons, especially at high temperatures [20,21]. The experimentally measured superhydrophobic properties of the sample with different laser scanning speeds are shown in Fig. S2(b). Among all these cases, the obtained contact angle of CA = 154° ± 1.25° and sliding angle of SA = 4.5° ± 0.25° for the sample at V = 0.4 mm/s indicates it is more efficient SHP surface. Because of the atmospheric air trapping inside the microgrooves, water droplets on such material surfaces are developed into the Caxie-Baxter state, which can effectively resist seawater penetration and complete surface wetting [22–24]. It helps to repel the aggressive corrosive ions in the seawater from the fabricated surface. The long-term anti-corrosion performance of these structured surfaces in the seawater is studied by electrochemical analysis. The fabricated surfaces before and after immersing in the seawater were subjected to the thorough surface analysis.

3.2. Long-term Anti-corrosion performance in the seawater

For the practical seawater application, it is necessary to characterize the long-term anti-corrosion performance stability of the laser structured sample surfaces in the real seawater. Fig. 3(a) illustrates the corrosion potentials (E_{corr}) and I_{corr} obtained from the cathodic polarization curve by Tafel extrapolation. According to Ohm's law $I_{corr} = E/R_p$, E is the electric potential difference between the anode and cathode

Table 1
Important parameters extracted from the cyclic polarization curves.

Samples		I_{corr} ($nAcm^{-2}$)	R_p ($k\Omega cm^{-2}$)	CR $(mm/y)*10^{-3}$	CIE %
Before laser fabrication	Al-bare	1155.0	25.2	15.1	-
Immediately after the laser fabrication	1.0 mm/s	64.0	570	0.699	94.45
	0.8 mm/s	48.0	590	0.531	95.84
	0.6 mm/s	15.0	2250	0.209	98.70
	0.4 mm/s	3.0	13,800	0.041	99.74
After two months of the seawater immersing	1.0 mm/s	72.0	540	0.78	93.76
	0.4 mm/s	10.0	2321	0.139	99.13

in the corrosion reaction; R_p, being also the so-called polarization resistance, is a sum of the electrical resistance of the corrosive medium (R_e) and the metal sample immersed (R_m). For the laser fabricated sample, R_m is modulated by the thick oxide layer on the material surface induced by the femtosecond laser irradiation. As shown in Table 1, the measured polarization resistance increases significantly to a maximum value of $R_p = 13.8$ MΩ cm^{-2} for the laser-fabricated samples at V = 0.4 mm/s, which results in the lowest corrosion current of $I_{corr} = 3.0 \times 10^{-9}$nA cm^{-2} in the seawater for 180 min. Fig. 3(b) depicts the Nyquist diagrams for the bare and laser-fabricated samples, where the larger diameter of the semi-circle for the materials with the superhydrophobic property indicates the higher corrosion resistance for the fabricated surfaces.

The corrosion rate (*CR*) for all the samples studied here are estimated as follows:

$$CR(mm/yr) = \frac{3.27 \times 10^{-3} \times I_{corr} \times M}{ND} \quad (1)$$

where *M* is the relative molar mass of the material (g/equivalent), *D* for the density of the material, and *N* for the number of electrons. The corrosion inhibition efficiency *(CIE%)* of the sample is calculated by:

$$CIE\% = \frac{I_c - I_c^{'}}{I_c} \times 100 \quad (2)$$

where I_c and $I_c^{'}$ are the corrosion current densities before and after the surface modification. The *CIE%* of any sample equals the percentage reduction of the current density from the bare sample. The important parameters extracted from the cyclic polarization curves, including I_{corr}, *CR* and *CIE%* are given in Table1. The measured corrosion potential of E_{corr}, the anodic slope (β_a), and the cathodic slope (β_c) values for the bare and laser-fabricated superhydrophobic sample surfaces are given in Table S3. It shows that the laser fabricated surface with the scanning speed of V = 0.4 mm/s exhibits the better anti-corrosive property than other samples, associated with a corrosion rate of 0.041 × 10^{-3} mm/year and a reduced corrosion dynamic current rate by 99.74 % relative to the bare surface.

Additionally, the detailed surface morphology analysis and electrochemical measurements have been carried out to investigate the long-term anti-corrosion performance of the bare and structured samples. For that, we immersed the bare and the fabricated samples at the laser scanning speed of V = 1.0 mm/s and 0.4 mm/s into the real seawater for two months, and the measurements of their cyclic polarization and Nyquist curves are shown in Fig. 3(c) and (d). From the cyclic polarization curve, we can find that the anti-corrosive nature of the sample for V = 0.4 mm/s is better than those of V = 1.0 mm/s and bare samples. Similarly, in comparison to the results of V = 1.0 mm/s, the obtained *CR* and *CIE %* values for the condition of V = 0.4 mm/s are seen to reduce and improve, respectively (refer to Table.1). The corrosion inhibition nature of the seawater immersed surfaces (for the bare, 0.4 mm/s, and 1.0 mm/s samples) is further evaluated using the Nyquist curves obtained from electrochemical impedance spectroscopy. The diameter of the Nyquist curve corresponding to the case of V = 0.4 mm/s is significantly larger than those of other samples, which indicates the more durable corrosion resistance behaviour.

An equivalent circuit shown in an inset of Fig. 3(d) was fitted to identify the individual contribution for the overall corrosion resistance of the samples, which includes the electrolyte solution resistance, the electrical resistance of the sample surface, and the electric double-layer capacitance (*C*) that is due to the neutral barrier layer formation at the material-electrolyte interface (shown in Fig. 1(b)) [15]. The measured electrical resistance of the bare and fabricated (at 1.0 mm/s and 0.4 mm/s) samples are R_m = 10.27 kΩ, 54.09 kΩ, and 152.0 kΩ, respectively. Clearly, the corrosion resistance for the sample surface of V = 0.4 mm/s is three times larger than that of V = 1.0 mm/s, and it is around fifteen times larger than that of the bare surface. This resistance enhancement might be due to the laser-induced Al and Mg oxide layers. Apart from such oxide layers, the double-layer capacitive resistance also provides additional corrosion protection. The underlying mechanisms in the formation of these stable oxide layers and the double-layer capacitance are discussed in the next section in detail. The values of *C* are measured as 33.8 μF, 112.0 μF, and 138.0 μF for the bare, 1.0 mm/s, and 0.4 mm/s sample surfaces, respectively. The combined resistance of such double-layer capacitance and stable oxide layer yielded the better corrosion protection for the laser fabricated sample surfaces even after immersing in the seawater for two months.

The detailed analyses of surface morphology ascertain the durability of the laser-fabricated surface structures in the continuous corrosive medium interaction. As shown by SEM images in Fig. 4, the bare sample surface undergoes the gradual corrosion process due to the continuous seawater interaction, leading to the significant pitting corrosion after two months of immersion. In contrast, the sample surfaces fabricated at the scanning speed of V = 0.4 mm/s are utterly free from corrosion even after two months of the seawater immersion. However, a significant change of the surface contact angle from 154° ± 1.25° to 92.0° ± 1° was observed on the sample fabricated at V = 0.4 mm/s. This is because the superhydrophobic nature of such structured surfaces is destroyed by removing the deposited organic layer [15]. Figure S3 shows the photographs of the samples fabricated with the scanning speed of V = 0.4 mm/s, in which the laser-structured portions remain almost unaffected after the seawater immersion. At the same time, the peripheric untreated areas seem to gradually lose the lustrous nature of Al alloy because of the corrosion happening. It indicates that the high corrosion protection for the femtosecond laser fabricated sample with V = 0.4 mm/s is not easily deteriorated along with its surface wettability even after the long-time immersion. But the bare sample surface undergoes the severe destruction with the clear evidence of pitting failures. Thus, the superhydrophobic is not an only determining factor for the long-term anti-corrosion property of the material, which may arise from other reasons.

3.3. Underlying mechanisms for the long-term Anti-corrosion performance

To investigate the underlying mechanisms for the long-term anti-corrosion property, a detailed investigation of the laser-induced material change has been carried out through EDS, XRD, and TEM analyses. Figure S4 shows the measured weight concentration of Al, Mg, and O elements for the bare and fabricated samples before and after immersing in the seawater. It is seen that with slowing the laser scanning speed during the sample treatment, there is an increase for the amount of O element but a decrease for Al and Mg elements. A similar trend is also observed for the fabricated samples immersed in the seawater for two months.

The formation of more metal oxides on the laser fabricated surfaces is indicated by the increased O content, associated with the reduced amount of Al_3Mg_2 compared to the bare sample. At the scanning speed of V = 0.4 mm/s, the number of femtosecond laser pulses interacting with the material is about twice that of V = 1.0 mm/s, resulting in the higher amount deposition of the oxidized recast layer. This is confirmed by comparing the EDS mapping of the chemical components at the cross-section of the structured sample with different scanning speeds (shown in Fig. 5 and Fig. S5). From the distribution mappings of Al, O, Mg and C elements, we can find that the components O and C spread almost uniformly within the surface layer of both structured samples, which might indicate the absorption of some airborne hydrocarbons. The weight concentration presented in Table S4 compares the chemical components for the samples processed at two different scanning speeds of V = 1.0 mm/s and V = 0.4 mm/s, where the ratio of O/Mg indicating the amount of Mg oxide layer formation appears to be larger in the latter case. The distribution of surface components also indicates that the formation of the protective Al-Mg oxide layer with the recast deposition up to tens of micrometers is stronger at the condition of V = 0.4 mm/s. It

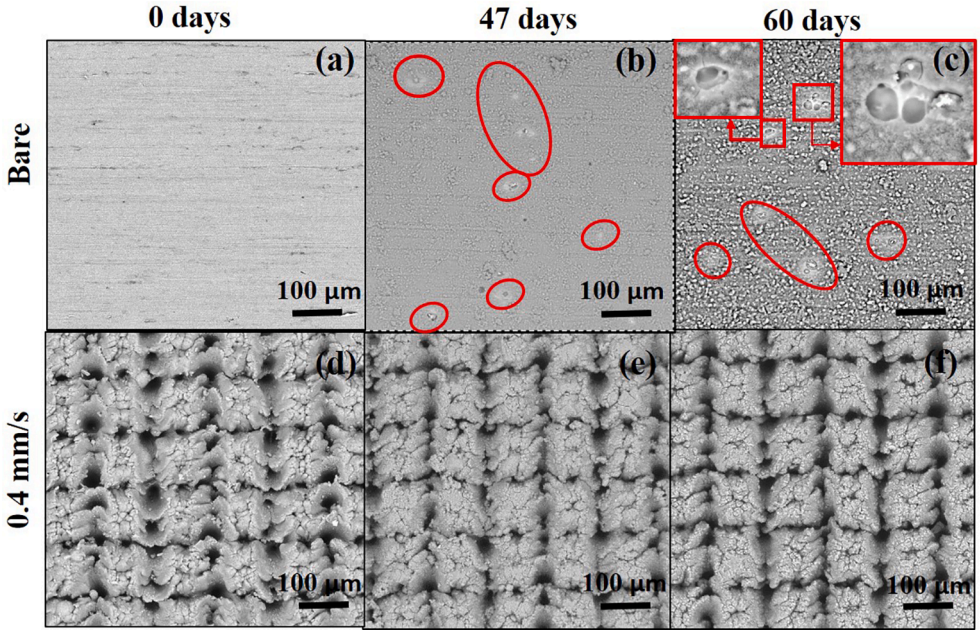

Fig. 4. Evolution of the surface morphology for different samples with the time duration of seawater immersion. (a-c) The bare sample, wherein the insets show the clear evidence of pitting due to aggressive corrosive ions; (d-f) for the laser fabricated sample with the scanning speed of V = 0.4 mm/s.

consequently prevents the diffusion of corrosive ions into the underneath substrate and greatly improves corrosion inhibition. Our results are consistent with the recent report by S. Adeosun *et al.*, where the weight concentration of Mg on Al alloys shows a significant effect on corrosion properties, and the lower Mg content provided the better anti-corrosive nature [25].

To analyze the laser-induced oxides and compounds in more detail, both the bare and the laser fabricated samples were subjected to the high-resolution (0.05 deg/min) XRD analysis. Fig. 6 shows the XRD peaks detected from these two surfaces, with the distinct peaks corresponding to different phases of Al_2O_3, MgO, and Al_3Mg_2. It suggests that the femtosecond laser irradiation can induce the thick layer of high stable oxides on the sample surface.

Interestingly, the femtosecond laser irradiation created the extreme physical conditions to accelerate the formation of thermodynamically stable α- Al_2O_3 on the sample surfaces. Due to its outstanding stability, α-Al_2O_3 is widely used as a protective coating material for metals. [26,27] Simultaneously, the presence of metastable phases such as γ-Al_2O_3 was also observed on the fabricated samples. Moreover, the previous studies also demonstrated that the high concentration of β-Al_3Mg_2 can help to increase the corrosive nature of Al-Mg alloys [25,28]. And Pierluigi Traverso et al. reported that the corrosion of Al-Mg alloys is like to decrease due to the formation of the Mg-Al oxide layer, which is more protective than Al hydroxides [29]. We observed that the high content of Al_3Mg_2 in the bare sample is decreased with smaller laser scanning speeds, as shown in Fig. 7(a), which provides the minimum value at V = 0.4 mm/s. The existence of Al, Al_2O_3, MgO, and Al_3Mg_2 on the laser fabricated samples was also confirmed through the electron diffraction pattern shown in the following section.

Another significant point to concern is the electrostatic reaction at the sample-electrolyte interface where the corrosion takes place. Due to the long-term immersion of the laser fabricated materials in the seawater, the positively charged surface of metals/ oxides electrostatically attracts aggressive ions such as Cl^-, Na^+, K^+ and OH^- from the electrolyte. Among them, the hydroxide (OH^-) anions show the higher adsorption energy and saturation coverage than others [30–32]. The immediate reaction of hydroxide ions with the surface tends to form a neutral barrier layer at the interface, which develops a double-layer capacitance and depletes the anion distribution in the vicinity of sample surfaces. Eventually, such a chemisorbed molecular layer introduces a strong barrier for the corrosive ion diffusion into the substrate. It suppresses the charge transfer between the possible anodic and cathodic sites confirmed through the electrochemical measurements. The measured corrosion current flow between the sample fabricated at V = 0.4 mm/s and the electrolyte is as small as 10 nA/cm^2. It resulted in an excellent long-term anti-corrosion performance after immersing in the seawater for 60 days, with a corrosion rate of 0.139×10^{-3} mm/yr and CIE of 99.74%. Thus, the formation of Al_2O_3 and MgO layers decreased the adsorption of corrosive cations from electrolytes and inhibited the cathodic and anodic reactions presented in Fig. 1(b), which helps to improve the anti-corrosion performance of the laser fabricated surface.

More importantly, the phase change from the crystallinity (long-range periodic arrangement of crystal lattice) to the partial amorphization in the fabricated samples was observed by XRD and TEM analyses, which can help to divulge the significant long-term anti-corrosive nature of Al alloy samples upon the femtosecond laser irradiation. As seen from the detected XRD peaks in Fig. 6, a broad peak appearing within a range of 23.45° − 34.50° indicates the material phase transformation from the crystalline to the amorphous [33]. The detailed information about the peak broadening and the intensity change of the major Al planes (111), (200), (220) and (311) are shown in Fig. S6, and they are well fitted by Lorentzian curves. For all the fabricated samples, the measured XRD peaks would like to show some distinct features, such as the significant broadening, a shift in the peak position, and the intensity change. In the case of each sample, the calculated full-width-half-maximum (FWHM) values for four different crystalline planes are shown in Fig. 7(b). The broadening of XRD peaks becomes pronounced with slower laser scanning speeds. For example, an inset in Fig. 7(b) shows the measured XRD peaks corresponding to Al (111) plane of the bare sample, and the sample fabricated at V = 0.4 mm/s. It is seen that the peak position of the fabricated sample (at V = 0.4 mm/s) shifts from $2\theta = 38.54°$ to 38.57° with the FWHM broadening of 0.162° to 0.206°, respectively, with respect to the bare sample. Fig. 7(c) shows the evolution of the crystallite sizes of Al for different crystalline planes, i.e. (111), (200), (220), and (311) with varying laser scanning speeds. Such peak position shift and broadening indicate that the femtosecond laser irradiation can modify the crystallite dimensions in different

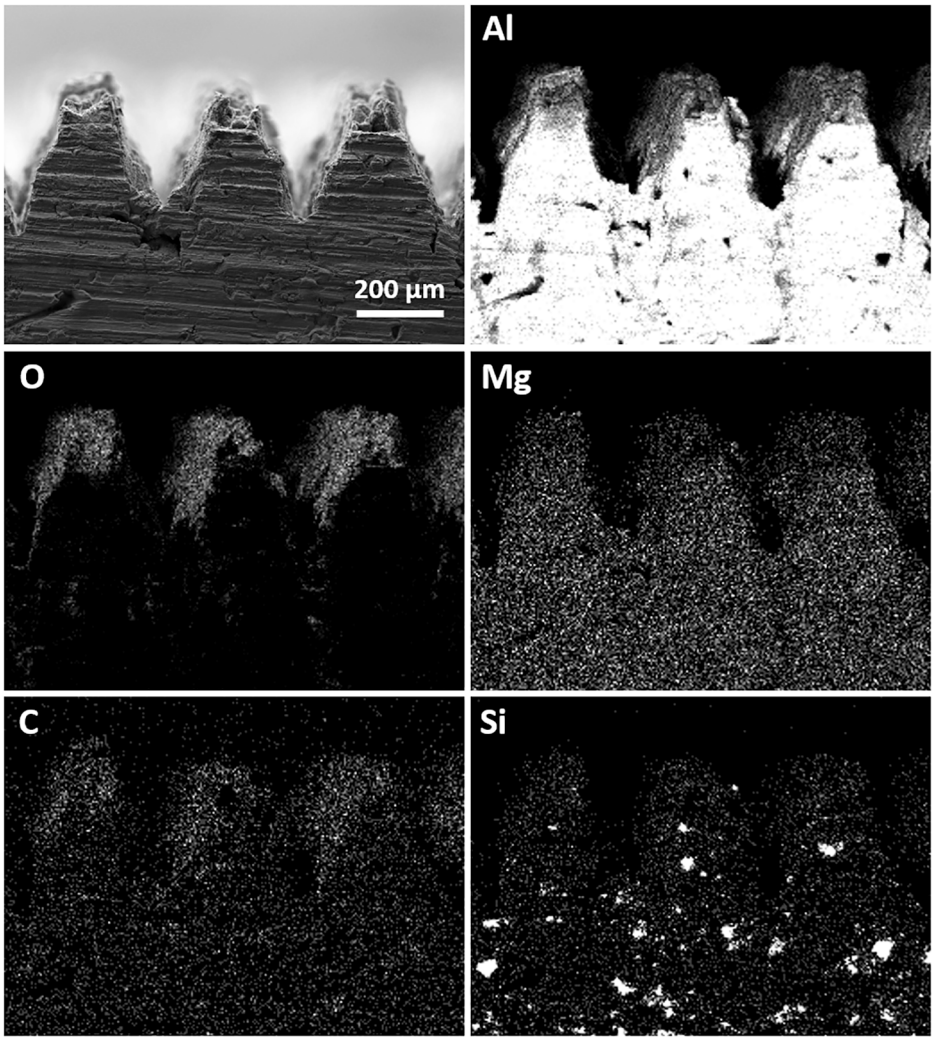

Fig. 5. Micro-analysis of the chemical components for the sample processed with the higher scanning speed of V = 0.4 mm/s by EDS mapping.

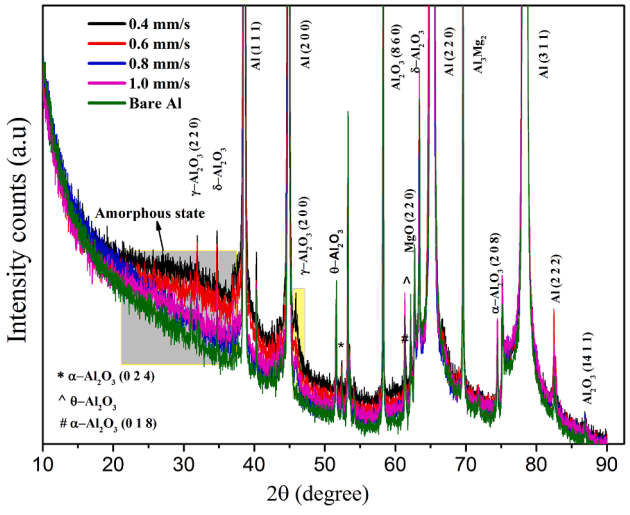

Fig. 6. Meaured XRD peaks for the laser fabricated sample surfaces with different scanning speeds. The highlighted areas at the lower values of 2θ indicate the amorphization of the samples.

crystalline planes. Fig. 7(d) shows that the lattice parameters and crystallinity of the fabricated samples are decreased with reducing the laser scanning speed. The maximum change of the lattice constant appears to take place for the fabricated samples with V = 0.4 mm/s. Under such circumstances, a great number of laser pulse irradiations can make the surface mechanical micro-deformation accumulated, which subsequently decreases the crystallinity from 99.56% (bare sample) to 92.36%.

According to Ref [38], the aforementioned changes in XRD peaks can be mainly attributed to the residual microstrain (ε) due to the crystal lattice dislocations and modulations in the crystallite size (L). In our case, the intense femtosecond laser irradiation can induce an inhomogeneous crystallite dislocation, leading to a strong distortion in the crystal lattice. An inhomogeneous strain arises (a combination of the compressed and the tensile strain) in the material, where the crystallites are strained differently and then shift the x-ray diffraction at different degrees. In the case of the strained crystallite, the interplanar spacing (d) will be changed, that is, it can be reduced by the compressed strain or increased by the tensile strain. It was observed that the broadened XRD peak for the fabricated samples shifted towards the higher angle (see the inset of Fig. 7(b)), which indicates that more compressed stress rather than tensile stress is generated by the laser processing, thus reducing the possibility of the crack formation or corrosion.

Consequently, because of the strong femtosecond laser interaction, changes in L and ε values are simultaneously contributing to the XRD

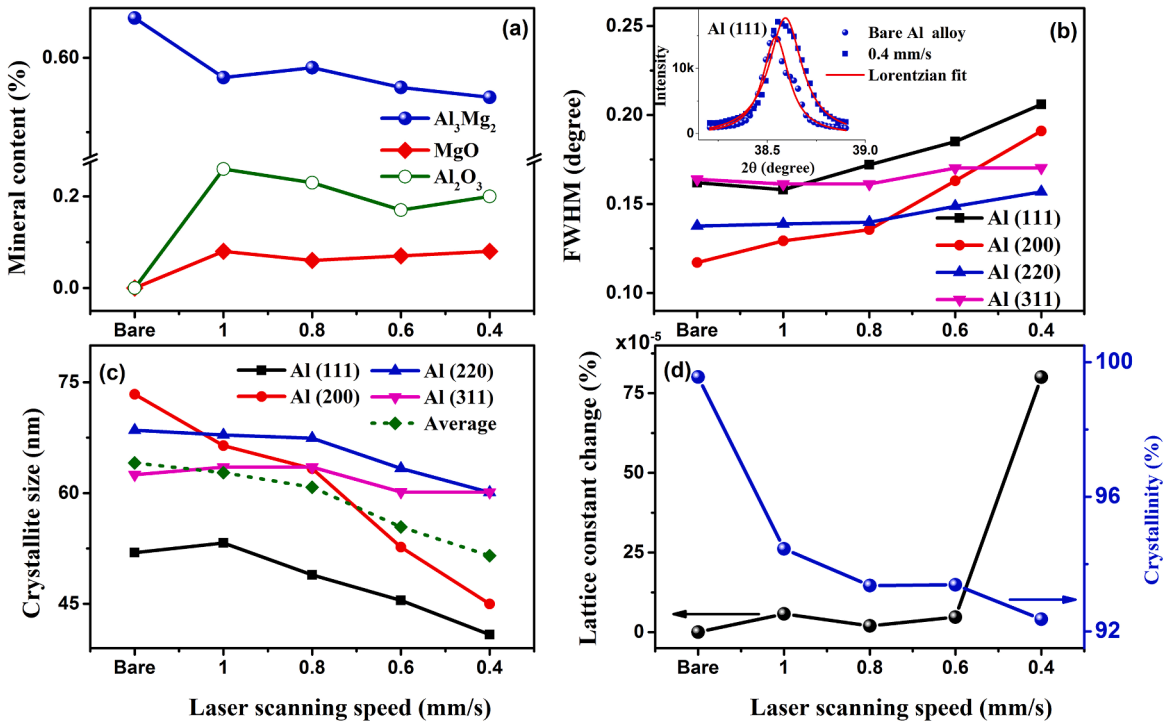

Fig. 7. Characterization of the bare and fabricated sample surfaces with different scanning speeds (V = 0.4 mm/s,0.6 mm/s 0.8 mm/s and 1.0 mm/s) using the XRD measurements. (a) Identified mineral contents of Al_3Mg_2, MgO and Al_2O_3, on the bare and laser fabricated samples; (b) peak broadening of various Al phases measured from FWHM (inset image shows the Lorentzian fitted peaks of Al (1 1 1) plane for both the bare and the laser fabricated samples at V = 0.4 mm/s), (c) variation of the grain size for the crystalline planes with different scanning speeds. (d) Amount of crystallinity change in the lattice constant with various laser scanning speeds.

peaks broadening. As explained in the supplementary information (Williamson-Hall (W-H) analysis on the XRD peak broadening), the total XRD peak broadening is a convolution of the individual broadening effects such as the residual microstrain and the crystallite size change (i.e, $\beta_{total} = \beta_L + \beta_\varepsilon$). A distinctive identification of the above two effects can be achieved by W-H analysis, which is expressed as follows [34,35]:

$$\beta_{total} cos\theta = 4\varepsilon\, sin\theta + \frac{K\lambda}{L} \quad (3)$$

Fig. 8 (a) shows the W-H plot for the studied samples, where the slope of the fitted line gives the magnitude of microstrain, and the Y-intercept values provide the crystallite size information (presented in Table S5). It illustrates that the magnitudes of microstrain in the fabricated samples are varied for different crystalline directions. The obtained mean microstrain value of $\varepsilon = 479 \times 10^{-6}$ for the fabricated sample at V = 0.4 mm/s is higher than those of other samples (i.e., $\varepsilon = 403 \times 10^{-6}$, 275×10^{-6}, 274×10^{-6} and 186×10^{-6} for the fabricated samples at V = 0.6 mm/s, 0.8 mm/s, 1.0 mm/s, and the bare sample, respectively). It shows that a mechanical micro-deformation of the crystal is yielded by the femtosecond laser irradiation, leading to the decreased grain sizes, crystallite sizes, and crystallinity in the fabricated samples. As a matter of fact, such kind of laser-induced deformation can

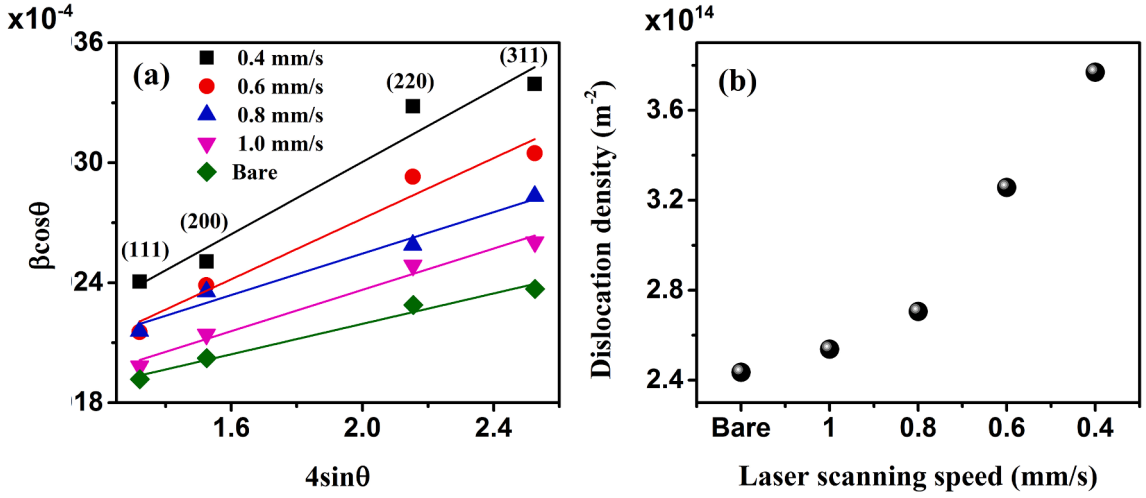

Fig. 8. Plots represents (a) W-H plots of βcosθ versus 4sinθ to calculate the crystallite size and lattice strain for bare and laser structured surfaces at various laser scanning speed and (b) shows the variation of crystalline dislocation density developed through femtosecond laser-induced strain.

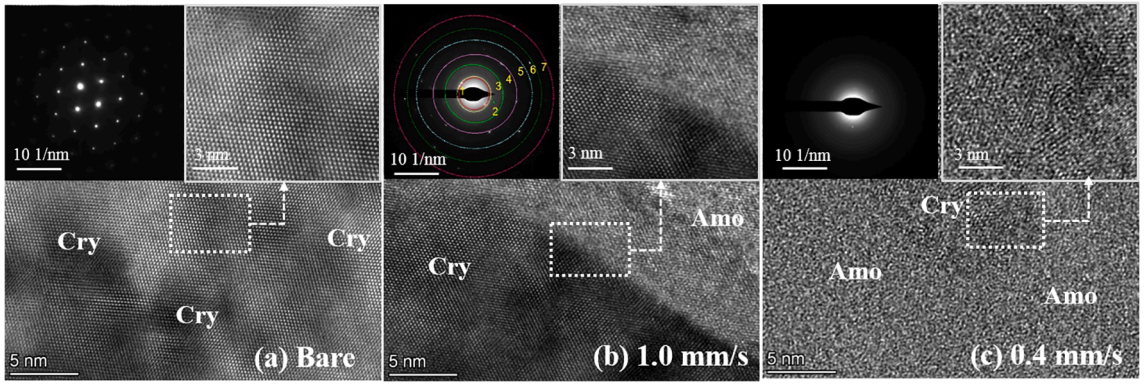

Fig. 9. Measured high-resolution TEM, SAED images (inset- left) of different samples. (a) For the bare sample with the clear lattice line orientation; (b)-(c) For the laser fabricated samples at V = 1.0 mm/s and 0.4 mm/s, respectively (the numbered circles in the inset are given as follows: 1 for 0.2434 nm MgO, 2for 0.240 nm Al_2O_3, 3for 0.2098 nm MgO, 4for 0.1702 nm Al_2O_3, 5for 0.093 nm Al, 6for 0.0808 nm Al_2O_3, 7for 0.0272 nm Al). Here the marked Cry areas and Amo represent the crystalline and amorphous regions, respectively.

be further understood by the dislocation density (δ), which is defined as a length of dislocation lines per unit volume of the crystal and can be evaluated using the following equation [36,37]:

$$\delta = \frac{1}{D^2} \tag{4}$$

where D is the average crystallite size mentioned in Fig. 7(c). The crystallite size of the fabricated samples is reduced by femtosecond laser-induced compressed strain to result in significant dislocation in the crystalline periodicity. Fig. 8(b) shows the calculated dislocation density of crystallites for different samples, and the obtained higher value at the condition of V = 0.4 mm/s implies the improvement of the material hardness [38]. Such an increased dislocation density inside the samples consequently turned the material phase from the crystalline into the partial amorphization.

Furthermore, the deep analyses of the crystal structure change for different samples are also carried out by a high-resolution TEM (HRTEM), and the results are presented in Fig. 9, with the corresponding surface area electron diffraction (SAED) patterns (upper-left insets). The results confirm a decrease in the crystallinity for the laser fabricated materials and the amorphous phase enhancement when reducing the laser scanning speed. As shown in Fig. 9(a), the lattice lines are evident for the bare sample whose corresponding electron diffraction pattern indicates a pure cubic crystalline phase belonging to the crystallographic space group of $FD3^{-}m$. However, for the fabricated samples at V = 1.0 mm/s and 0.4 mm/s, the regular arrangement of lattice lines is disturbed, as shown in Fig. 9 (b) and (c), indicating the crystallite dislocation occurred after the femtosecond laser processing. Such distortion and amorphization can be considered from the influence of the non-uniform stress and strain induced by femtosecond laser pulse irradiation because after the femtosecond laser ablation process, a thin layer of material is promoted to melt by the residual pulse energy and abruptly cooldown without re-crystallization [39]. It is similar to the method of melt quenching (a widely used fabrication method of amorphous metals) to transform the crystalline material into an amorphous state [40]. Therefore, either a diffused halo or a circular electron diffraction pattern can be evidenced from the fabricated samples as shown in the SAED images. The numbered circular electron diffraction rings in Fig. 9(b) confirm the presence of MgO, Al_2O_3, and Al on the fabricated sample surfaces. Concurrently the bright central halos in SAED patterns of Fig. 9(b) and 9(c) can identify the decrement in the material crystallinity even into the partial amorphous state. From the observation in HRTEM images, we can clearly see the disordered crystal lattice lines with the amorphous surroundings, which suggests the maximum material phase change for the sample fabricated at V = 0.4 mm/s.

As reported before [41], the amorphization of a polycrystalline metal alloy would like to decrease the microstructural features of the material, such as grain boundaries, defect sites, and chemical inhomogeneity, all of which are favorable nucleation sites of corrosions because they can act as anodic spots. Moreover, the laser induced dislocation densities decrease the free energy within the amorphized material, thus leading to the increased chemical stability of metal alloys to decrease the reactivity of the elements [42,43]. Hence, the partial amorphization of Al alloy sample by the femtosecond laser processing would like to introduce the considerable R_p and decrease the I_{corr} between the galvanic pairs, which greatly reduces the overall *CR* for these surfaces, specifically for the situation at V = 0.4 mm/s.

4. Conclusion

We have proposed a novel efficient strategy of femtosecond laser-induced phase change to improve the long-term anti-corrosion properties of Al alloy surface. At first, the sample surfaces were struck by the infrared femtosecond laser pulses (1 kHz, 800 nm and 40 fs) at different scanning speeds to generate the micro/nano-structures. Subsequently, they are treated by the simple annealing process to achieve the superhydrophobic phenomenon. The electrochemical measurements in the seawater environment revealed that the fabricated sample at the low laser scanning speed of V = 0.4 mm/s would like to exhibit the better-improved corrosion resistance (13.8 $M\Omega/cm^2$) when compared with other scanning speeds and the bare sample (25.2 $k\Omega/cm^2$). Most importantly when we immersed the fabricated samples in the seawater for two months, the obtained optimal long-term corrosion inhibition efficiency can reach as high as 99.13%.

To explore the intrinsic mechanism involvement, we have examined the material changes from different aspects including the chemical composition and the crystalline lattice, and found the significance of oxides formation and the crystal-amorphous phase transformation on the pronounced anti-corrosion behaviors. In general, the observed anti-corrosive property of femtosecond laser-treated samples can be attributed to the following points: (i) the superhydrophobic effect of the micro air cavities on the surface structures, (ii) thick and stable Al-Mg oxide layer formation and (iii) the amount of phase change from crystalline to amorphous. It is noticed that the latter two factors are mainly responsible for the long-term anti-corrosion observations. This study has provided new insights into the femtosecond laser processing of Al alloy surfaces for the great improvement of anti-corrosion properties, which can be extendable for other metal surfaces and will have a promising future of development in practical applications.

CRediT authorship contribution statement

Rahul A. Rajan: Writing – original draft, Methodology, Investigation, Formal analysis, Writing – review & editing. **Srinivasa Rao Konda:** Data curation, Writing – review & editing. **Chaudry Sajed Saraj:** Investigation. **Yu Hang Lai:** Resources. **Gopal Verma:** Formal analysis. **Zhi Yu:** Resources, Project administration. **Weili Yu:** Resources. **Dandan Yan:** Resources. **Jianjun Yang:** Conceptualization, Writing – review & editing, Supervision, Project administration, Funding acquisition.

Declaration of Competing Interest

The authors declare that they have no known competing financial interests or personal relationships that could have appeared to influence the work reported in this paper.

Acknowledgement

This research was financially supported by the Strategic Priority Research Program of Chinese Academy of Sciences (No. XDA22010302), National Natural Science Foundation of China (Grant Nos. 91750205, 11674178), Jilin Provincial Science & Technology Development Project (Grant No. 20180414019GH, 20200201086JC), and the K. C. Wong Education Foundation (GJTD-2018-08). S.R. Konda acknowledges his support by the Chinese Academy of Sciences President's International Fellowship Initiative (grant no. 2021PM0036), and Rahul A. Rajan gratefully acknowledges his support from UCAS Full-Fellowship for International Students (20190442).

Appendix A. Supplementary material

Supplementary data to this article can be found online at https://doi.org/10.1016/j.apsusc.2021.151612.

References

[1] S. Das, Development of aluminium alloy composites for engineering applications, Trans. Indian Inst. Met. 57 (2004) 325–334.
[2] W. Jurczak, Study of the corrosion resistance of ship aluminium alloys, Zesz. Nauk. Akad. Mar. Wojennej. 206 (2016) 37–65.
[3] M.A. Wahid, A.N. Siddiquee, Z.A. Khan, Aluminum alloys in marine construction: characteristics, application, and problems from a fabrication viewpoint, Mar. Syst. Ocean Technol. 15 (1) (2020) 70–80, https://doi.org/10.1007/s40868-019-00069-w.
[4] M. Moukwa, Penetration of Chloride Ions From sea Water into Mortars Under Different Exposure Conditions, Cem. Concr. Res. 19 (6) (1989) 894–904.
[5] R. Yuan, S. Wu, P. Yu, B. Wang, L. Mu, X. Zhang, Y. Zhu, B. Wang, H. Wang, J. Zhu, Superamphiphobic and Electroactive Nanocomposite toward Self- Cleaning, Antiwear, and Anticorrosion Coatings, ACS Appl. Mater. Interfaces. 8 (19) (2016) 12481–12493.
[6] Y. Shen, Z. Wu, J. Tao, Z. Jia, H. Chen, S. Liu, J. Jiang, Z. Wang, Spraying Preparation of Eco-Friendly Superhydrophobic Coatings with Ultralow Water Adhesion for Effective Anticorrosion and Antipollution, ACS Appl. Mater. Interfaces. 12 (22) (2020) 25484–25493.
[7] L.R. de Lara, R. Jagdheesh, J.L. Ocaña, Corrosion resistance of laser patterned ultrahydrophobic aluminium surface, Mater. Lett. 184 (2016) 100–103, https://doi.org/10.1016/j.matlet.2016.08.022.
[8] L.B. Boinovich, A.M. Emelyanenko, A.D. Modestov, A.G. Domantovsky, K. A. Emelyanenko, Synergistic Effect of Superhydrophobicity and Oxidized Layers on Corrosion Resistance of Aluminum Alloy Surface Textured by Nanosecond Laser Treatment, ACS Appl. Mater. Interfaces. 7 (34) (2015) 19500–19508.
[9] W.J. Wang, K.C. Yung, H.S. Choy, T.Y. Xiao, Z.X. Cai, Effects of laser polishing on surface microstructure and corrosion resistance of additive manufactured CoCr alloys, Appl. Surf. Sci. 443 (2018) 167–175, https://doi.org/10.1016/j.apsusc.2018.02.246.
[10] F. Chen, D. Zhang, Q. Yang, J. Yong, G. Du, J. Si, F. Yun, X. Hou, Bioinspired Wetting Surface via Laser Microfabrication, ACS Appl. Mater. Interfaces. 5 (15) (2013) 6777–6792.
[11] X. Xun, R. Zhu, J. Dong, T. Pan, M. Zhong, R. Zhang, D. Zang, Superhydrophobic Light Alloy Materials with Corrosion-Resistant Surfaces, Res. Appl. Mater. Sci. 2 (2020) 1–11.
[12] L.B. Boinovich, E.B. Modin, A.R. Sayfutdinova, K.A. Emelyanenko, A.L. Vasiliev, A. M. Emelyanenko, Combination of Functional Nanoengineering and Nanosecond Laser Texturing for Design of Superhydrophobic Aluminum Alloy with Exceptional Mechanical and Chemical Properties, ACS Nano. 11 (10) (2017) 10113–10123.
[13] M. Rafieazad, J. Jaffer, C. Cui, X. Duan, A. Nasiri, Nanosecond laser fabrication of hydrophobic stainless steel surfaces: The impact on microstructure and corrosion resistance, Materials (Basel). 11 (9) (2018) 1577, https://doi.org/10.3390/ma11091577.
[14] Y. Yang, Y. Chen, J. Zhang, X. Gu, P. Qin, N. Dai, X. Li, J.P. Kruth, L.C. Zhang, Improved corrosion behavior of ultrafine-grained eutectic Al-12Si alloy produced by selective laser melting, Mater. Des. 146 (2018) 239–248, https://doi.org/10.1016/j.matdes.2018.03.025.
[15] L.B. Boinovich, A.M. Emelyanenko, A.D. Modestov, A.G. Domantovsky, K. A. Emelyanenko, Not simply repel water: the diversified nature of corrosion protection by superhydrophobic coatings, Mendeleev Commun. 27 (3) (2017) 254–256, https://doi.org/10.1016/j.mencom.2017.05.012.
[16] C.V. Ngo, D.M. Chun, Control of laser-ablated aluminum surface wettability to superhydrophobic or superhydrophilic through simple heat treatment or water boiling post-processing, Appl. Surf. Sci. 435 (2018) 974–982, https://doi.org/10.1016/j.apsusc.2017.11.185.
[17] Copernicus, (n.d.). https://resources.marine.copernicus.eu/?option=com_csw&view=order&record_id=9fe675d9-794a-46a1-abcb-471fa4279d2b.
[18] H. Choi, H. Liang, Wettability and spontaneous penetration of a water drop into hydrophobic pores, J. Colloid Interface Sci. 477 (2016) 176–180, https://doi.org/10.1016/j.jcis.2016.05.029.
[19] G. Verma, C.S. Saraj, G. Yadav, S.C. Singh, C. Guo, Generalized emptying criteria for finite-lengthed capillary, Phys. Rev. Fluids. 5 (2020) 112201–112209.
[20] R.A. Rajan, C.-V. Ngo, J. Yang, Y.u. Liu, K.S. Rao, C. Guo, Femtosecond and picosecond laser fabrication for long-term superhydrophilic metal surfaces, Opt. Laser Technol. 143 (2021) 107241, https://doi.org/10.1016/j.optlastec.2021.107241.
[21] D. Huerta-Murillo, A.I. Aguilar-Morales, S. Alamri, J.T. Cardoso, R. Jagdheesh, A. F. Lasagni, J.L. Ocaña, Fabrication of multi-scale periodic surface structures on Ti-6Al-4V by direct laser writing and direct laser interference patterning for modified wettability applications, Opt. Lasers Eng. 98 (2017) 134–142, https://doi.org/10.1016/j.optlaseng.2017.06.017.
[22] K. Ding, M. Li, C. Wang, N. Lin, H. Wang, Z. Luo, J. Duan, Sequential Evolution of Colored Copper Surface Irradiated by Defocused Femtosecond Laser, Adv. Eng. Mater. 22 (10) (2020) 1901310, https://doi.org/10.1002/adem.v22.1010.1002/adem.201901310.
[23] K. Ding, C. Wang, Y. Zheng, Z. Xie, Z. Luo, S. Man, B. Wu, J. Duan, One-step fabrication of multifunctional fusiform hierarchical micro/nanostructures on copper by femtosecond laser, Surf. Coatings Technol. 367 (2019) 244–251, https://doi.org/10.1016/j.surfcoat.2019.04.005.
[24] Y. Song, C. Wang, X. Dong, K. Yin, F. Zhang, Z. Xie, D. Chu, J. Duan, Controllable superhydrophobic aluminum surfaces with tunable adhesion fabricated by femtosecond laser, Opt. Laser Technol. 102 (2018) 25–31, https://doi.org/10.1016/j.optlastec.2017.12.024.
[25] S.O. Adeosun, O.I. Sekunowo, S.A. Balogun, V.D. Obiekea, Corrosion behaviour of heat-treated aluminum-magnesium alloy in chloride and EXCO environments, Int. J. Corros. 2012 (2012), 927380.
[26] S.D. Ponja, I.P. Parkin, C.J. Carmalt, Synthesis and material characterization of amorphous and crystalline (α-) Al2O3: Via aerosol assisted chemical vapour deposition, RSC Adv. 6 (2016) 102956–102960.
[27] M.H. Hussin, N.A. Che Lah, Effects of temperature on the surface and subsurface of Al-Mg-Si welded joints, J. Mech. Eng. Sci. 11 (2) (2017) 2743–2754.
[28] Y. Li, J.M. Cai, L. Guan, G. Wang, pH-dependent electrochemical behaviour of Al 3 Mg 2 in NaCl solution, Appl. Surf. Sci. 467-468 (2019) 619–633.
[29] P. Traverso, E. Canepa, A review of studies on corrosion of metals and alloys in deep-sea environment, Ocean Eng. 87 (2014) 10–15.
[30] M. Kosmulski, Compilation of PZC and IEP of sparingly soluble metal oxides and hydroxides from literature, Adv. Colloid Interface Sci. 152 (1-2) (2009) 14–25, https://doi.org/10.1016/j.cis.2009.08.003.
[31] C.S. Tian, Y.R. Shen, Structure and charging of hydrophobic material/water interfaces studied by phase-sensitive sum-frequency vibrational spectroscopy, Proc. Natl. Acad. Sci. U. S. A. 106 (36) (2009) 15148–15153.
[32] P. Creux, J. Lachaise, A. Graciaa, J.K. Beattie, A.M. Djerdjev, Strong specific hydroxide ion binding at the pristine oil/water and air/water interfaces, J. Phys. Chem. B. 113 (43) (2009) 14146–14150.
[33] Y. Zhang, L. Liu, G. Zou, N. Chen, A. Wu, H. Bai, Y. Zhou, Femtosecond laser-induced phase transformations in amorphous Cu77Ni6Sn10P7 alloy Femtosecond laser-induced phase transformations in amorphous, J. Appl. Phys. 023109 (2015) 2–7.
[34] G.K. Williamson, W.H. Hall, X-ray line broadening from filed aluminium and wolfram, Acta Metall. 1 (1) (1953) 22–31.
[35] V. Mote, Y. Purushotham, B. Dole, Williamson-Hall analysis in estimation of lattice strain in nanometer-sized ZnO particles, J. Theor. Appl. Phys. 6 (2012) 2–9.
[36] V. Bilgin, S. Kose, F. Atay, I. Akyuz, The effect of substrate temperature on the structural and some physical properties of ultrasonically sprayed CdS films, Mater. Chem. Phys. 94 (1) (2005) 103–108.
[37] Z.R. Khan, M. Zulfequar, M.S. Khan, Optical and structural properties of thermally evaporated cadmium sulphide thin films on silicon (1 0 0) wafers, Mater. Sci. Eng. B Solid-State Mater. Adv. Technol. 174 (1-3) (2010) 145–149, https://doi.org/10.1016/j.mseb.2010.03.006.
[38] D.C. Calhoun, R.B. Dunand, Dislocations in Metal Matrix Composites, Compr. Compos. Mater. 3 (2000) 27–59.

[39] S. Valette, R. Le Harzic, E. Audouard, N. Huot, R. Fillit, R. Fortunier, X-ray analysis of mechanical and thermal effects induced by femtosecond laser treatment of aluminum single crystals, Appl. Surf. Sci. 252 (13) (2006) 4691–4695.
[40] Y. Hirayama, M. Obara, Heat-affected zone and ablation rate of copper ablated with femtosecond laser, J. Appl. Phys. 97 (6) (2005) 064903, https://doi.org/10.1063/1.1852692.
[41] M. Naka, K. Hashimoto, A. Inoue, T. Masumoto, Corrosion Resistant Amorphous Fe-C Alloys Containing Chromium and/or Molybdenum, J. Non. Cryst. Solids. 37 (1980) 85–97.
[42] I. Majewska-Glabus, B.J. Thijsse, Calorimetric and Resistometric Studies of Structural Relaxation Kinetics in Fe40Ni4OP20 and Fe40Ni4OB20, Elsevier B.V. (1985), https://doi.org/10.1016/B978-0-444-86939-5.50152-4.
[43] C.A.C. Souza, F.S. Politi, C.S. Kiminami, Influence of structural relaxation and partial devitrification on the corrosion resistance of Fe78B13Si9 amorphous alloy, Scr. Mater. 39 (3) (1998) 329–334.